Exp Fluids (2015) 56:150
DOI 10.1007/s00348-015-2022-7

RESEARCH ARTICLE

A comparison of wake measurements in motor-driven and flow-driven turbine experiments

Daniel B. Araya[1] · John O. Dabiri[2]

Received: 17 February 2015 / Revised: 9 June 2015 / Accepted: 25 June 2015
© Springer-Verlag Berlin Heidelberg 2015

Abstract We present experimental data to compare and contrast the wake characteristics of a turbine whose rotation is either driven by the oncoming flow or prescribed by a motor. Velocity measurements are collected using two-dimensional particle image velocimetry in the near-wake region of a lift-based, vertical-axis turbine. The wake of this turbine is characterized by a spanwise asymmetric velocity profile which is found to be strongly dependent on the turbine tip speed ratio (TSR), while only weakly dependent on Reynolds number (*Re*). For a given *Re*, the TSR is controlled either passively by a mechanical brake or actively by a DC motor. We find that there exists a finite region in TSR versus *Re* space where the wakes of the motor-driven turbine and flow-driven turbine are indistinguishable to within experimental precision. Outside of this region, the sign of the net circulation in the wake changes as TSR is increased by the motor. Shaft torque measurements show a corresponding sign change above this TSR threshold set by circulation, indicating a transition from net torque due to lift to net torque due to drag produced by the turbine blades, the latter of which can give wake measurements that are inconsistent with a flow-driven turbine. The results support the claim that the turbine kinematics and aerodynamic properties are the sole factors that govern the dynamics of its wake, irrespective of the means to move the turbine blades. This has significance for both experimental and computational studies where it may be necessary, or perhaps more economical, to prescribe the turbine kinematics in order to analyze its aerodynamic characteristics.

✉ Daniel B. Araya
daraya@caltech.edu

John O. Dabiri
jodabiri@caltech.edu

[1] Graduate Aerospace Laboratories, California Institute of Technology, Pasadena, CA 91125, USA

[2] Graduate Aerospace Laboratories and Bioengineering, California Institute of Technology, Pasadena, CA 91125, USA

1 Introduction

When studying flow phenomena in a scaled laboratory experiment or in a computational simulation, it is often not possible to achieve dynamic similarity with the full-scale flow of interest. In the case of wind and water turbine experiments, a scaled model turbine may not perform as well as in the field, or perhaps not at all, due to a mismatch of Reynolds number and other scaling difficulties such as increased bearing friction. Grant and Parkin (2000) note that in very small-scale model turbine experiments, the blades may operate below their design Reynolds number, causing extensive flow separation that can limit the extrapolation of these model tests to full-scale rotors. Despite this, both wind and water tunnel experiments are used as a practical means to study the flow characteristics of turbines even when dynamic similarity cannot be achieved.

Recent progress has been made in understanding the aerodynamics of cross-flow turbines, also known as vertical-axis wind/water turbines (VAWTs). Bachant and Wosnik (2014) examined the effect of Reynolds number on the near-wake characteristics of VAWTs. They found that turbine performance becomes nearly independent of Reynolds number above turbine diameter Reynolds number of $Re_D = 8 \times 10^5$. They also observed that near-wake statistics, such as mean velocity and turbulence intensity, showed only slight differences across the full range of Reynolds number that was examined, i.e., $Re_D = 3\text{–}13 \times 10^5$.

Published online: 11 July 2015

Fujisawa and Shibuya (2001) as well as Ferreira et al. (2009) investigated the dynamic stall characteristics of VAWTs using an isolated turbine blade. To mimic the VAWT dynamics, they used a motor to rotate the blade about a central axis within a freestream flow and observed the successive generation and shedding of vortices from the blade as it was rotated. Both studies concluded that the development of these vortices changed as the tip speed ratio (TSR), i.e., the ratio of blade speed to freestream flow speed, was increased, but neither made reference as to whether such observations were physical with respect to a functional VAWT whose rotation is only driven by the oncoming flow.

This practice of prescribing the motion of turbine blades within a flow is common among both experimental and numerical turbine investigations. A survey of previous literature is tabulated in the "Appendix", with a distinction made between studies that used 'flow-driven' and 'motor-driven' turbines, details of which are provided in Sect. 2. The compilation highlights the frequent use of the motor-driven technique and also inconsistencies in reporting power or torque measurements, which is shown in the current work to be an important aspect of matching the wake characteristics of flow-driven turbines.

Intuitively, one might anticipate that a motor-driven turbine whose geometry, shaft torque, and TSR match that of a flow-driven turbine would also share the same performance and wake characteristics. However, this conjecture has not been experimentally tested. A recent computational study by Le et al. (2014) compared the performance of a flow-driven turbine subject to a given load with that of one whose TSR is specified. Their results show reasonable agreement in the measured power coefficient of the two configurations, which is consistent with the aforementioned hypothesis. Still, it remains unclear how the prescribed motion affects the resulting flow field measurements, e.g., the wake velocity profile and power spectra. In the present work, we use two-dimensional particle image velocimetry (PIV) to measure the velocity in the wake of a 3-bladed VAWT. We examine the average velocity, velocity power spectra, wake circulation, and measurements of shaft torque among various flow-driven and motor-driven configurations.

2 Description of experimental test cases

2.1 Flow-driven turbine

Under normal operating conditions, the rotation of a turbine rotor about its central axis is driven by the oncoming flow. In practice, this means that the turbine rotation rate is fixed by the torque due to aerodynamic forces as well as any additional applied load, such as bearing friction, an electrical generator, or, often in experiments, an unpowered DC motor used to model a generator (see, e.g., Kang and Meneveau 2010). In a numerical simulation, this additionally implies that the fully coupled fluid–structure interaction (FSI) is modeled for the turbine. Of the literature surveyed, relatively few researchers (see, e.g., Bazilevs et al. 2011; Hsu and Bazilevs 2012; Le et al. 2014) included the turbine FSI in their numerical simulations.

A schematic of the aerodynamic forces acting on a VAWT airfoil is shown in Fig. 1.

In the absence of any externally applied load, the turbine is free to spin to an average rate dependent solely on the balance of torque due to lift and drag of the blades. This is referred to henceforth as the 'free-spin' operating condition of the turbine and is shown schematically in Fig. 2.

Note that this condition is the theoretical upper bound on the average rotation rate for a given turbine geometry and flow Reynolds number. The addition of friction into the system or power extraction via an electrical generator serves to apply a torque in the direction opposing the

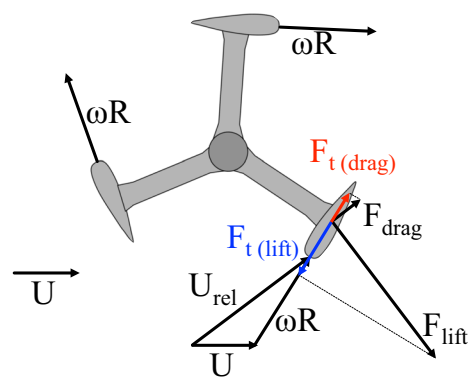

Fig. 1 Vector diagram of the aerodynamic forces acting on a VAWT airfoil. Here U is the freestream velocity ω is the angular velocity of the turbine, R is the turbine radius, U_{rel} is the relative freestream velocity as seen by the turbine blade, and $F_{\mathrm{t(lift)}}$ and $F_{\mathrm{t(drag)}}$ are the tangential components of the lift and drag forces, i.e., F_{lift} and F_{drag}, respectively

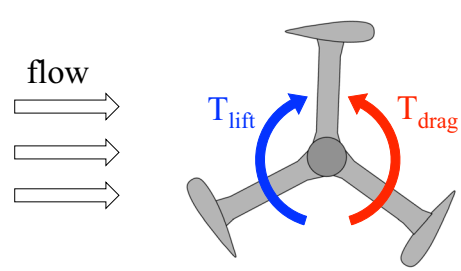

Fig. 2 Free-body diagram (*top view*) of a flow-driven VAWT for the free-spin operating condition. Here the net torque due to lift, T_{lift}, balances with the net torque due to drag, T_{drag}

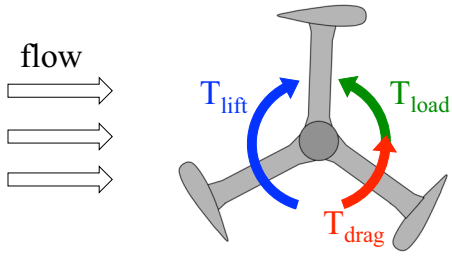

Fig. 3 Free-body diagram (*top view*) of a flow-driven VAWT operating with an applied load. Here the net torque due to lift, T_{lift}, of the blades exceeds the torque due to drag, T_{drag}, and is balanced by the torque added by an applied load, T_{load}

torque due to lift, as indicated in Fig. 3, which slows the turbine to a new, lower equilibrium rotation rate.

2.2 Motor-driven turbine

A scaled turbine often cannot produce sufficient torque to reach the TSR observed at full scale. This could be the result of excessive friction in the system, reduced aerodynamic performance at the Reynolds number of the scaled turbine, or perhaps because an isolated blade is being investigated. Regardless, it often leads to the use of a motor to actively drive the motion of the turbine blade(s). A similar practice is common in numerical turbine simulations where the blade kinematics is specified but the dynamic fluid–structure interaction is neglected to reduce computational costs. By using a motor in an experiment, additional forces are applied to the turbine system. In particular, the motor itself has a finite amount of internal resistance that results in a torque in the same direction as the aerodynamic drag on the turbine blades. Thus, in order to rotate the turbine shaft, power must first be supplied to the motor to overcome its own resistance and further power must be supplied to accelerate the turbine shaft. It is important to emphasize, however, that the lift and drag produced by the oncoming flow past the blades is always present, regardless of the motor. Therefore, it is the sum of all of these forces that determines the kinematics of the turbine, as illustrated in Fig. 4.

During steady operation, the motor can control the turbine rotation within three distinct operational regimes: (a) a lift-dominated regime, wherein the net torque due to aerodynamic lift on the blades exceeds the net torque due to drag and the motor effectively acts as a generator to mimic power extraction in a flow-driven case, (b) a neutral regime, wherein the net torque due to aerodynamic lift of the blades is balanced by the torque due to drag (i.e., the free-spin condition), and the motor only acts to overcome its own internal resistance, and (c) a drag-dominated regime, wherein the net torque due to aerodynamic drag of

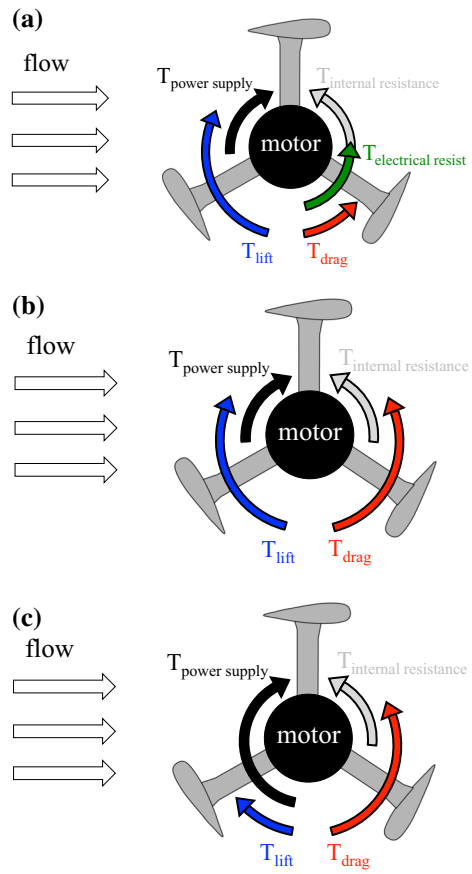

Fig. 4 Free-body diagram of the motor-driven turbine when operating in, **a** the lift-dominated regime, **b** the neutral regime, and **c** the drag-dominated regime. The components of torque that contribute to the overall shaft torque are shown in each regime with *colored arrows*. Note that only torques due to the motor and aerodynamics are considered, i.e., friction is neglected

the blades exceeds the torque due to lift and the motor acts to accelerate the turbine to a rotation rate that it could not achieve under flow-driven conditions alone. These three regimes are shown schematically in Fig. 4a–c, respectively. In our experiment, we evaluated the turbine wake characteristics across all three regimes and compared with flow-driven cases when possible.

3 Experimental setup

3.1 Model turbine

A three-bladed model turbine was 3D printed for the experiment using a polycarbonate-like material (3D Systems Accura® 60 Plastic). The printed model was sanded and bead-blasted to 320-grit, giving a smooth surface finish. Figure 5 shows a CAD drawing of the turbine along with relevant dimensions. Each of the three turbine blades

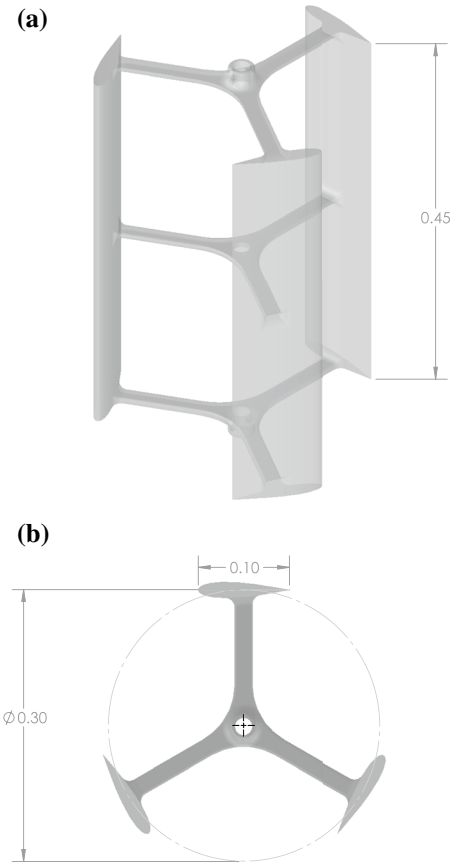

Fig. 5 CAD drawing of the model turbine used in the experiment. **a** Isometric view and **b** top view. All dimensions are given in meters

consisted of a NACA 0018 airfoil with a 0.1-m chord and extruded to a length of 0.45 m. The turbine diameter was 0.3 m, as measured by a circle tangent to the chord of each airfoil. The turbine blockage ratio, based on its frontal projected area, varied between 8–16 % over one revolution.

3.2 Water channel facility

Experiments were conducted in a 40-m-long, 1.1-m-wide, and 0.6-m-deep, free surface, recirculating water channel facility capable of flow speeds up to approximately 26 cm^{-1}. The bottom end of the turbine central shaft was attached to a flange mount with Type 316 stainless steel ball bearings. This flange was mounted to a stainless steel plate that anchored the turbine to the floor of the water channel. The top end of the turbine shaft was connected to a rotary torque sensor with digital encoder (Futek TRS705). The torque sensor had a 0–20 N-m measurement range with a maximum system error of +0.020 % rated output (i.e., +0.004 N-m) in clockwise torque and −0.025 % rated output (i.e., −0.005 N-m) in counterclockwise torque. An optically clear, cast acrylic sheet,

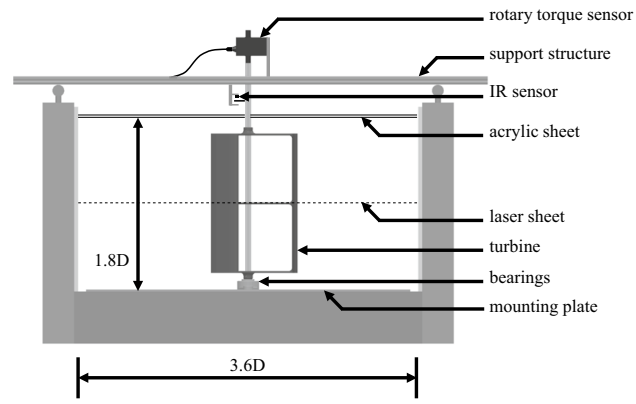

Fig. 6 Section view schematic of the experimental setup

approximately 1.8 m in length and spanning the width of the channel, was suspended to be flush with the free surface in order to eliminate surface distortion. A cross-sectional view of the model turbine mounted in the water channel is shown in Fig. 6.

3.3 Diagnostics

For particle image velocimetry (PIV), the flow was seeded with 100 μm silver-coated hollow ceramic spheres (Potters Industries LLC). To illuminate the particles, a collimated laser sheet was created in a plane parallel to the mid-height of the turbine using a continuous, 1W, 532-nm DPSS laser system (Laserglow Technologies) along with a single plano-concave cylindrical lens with a −3.9 mm focal length (Thorlabs) mounted directly in front of the laser. A custom-built infrared (IR) sensor was used to detect the starting orientation of the turbine for each data set.

The voltage signal from this IR sensor as well as from the torque sensor and encoder was input into a National Instruments data acquisition (NIDAQ) device (USB-6221), which was controlled by LabView software (National Instruments). Using the TTL signal from the encoder, the NIDAQ device triggered a high-speed camera (Photron APX-RS), mounted above the channel, to capture two images of the turbine wake every 5° of shaft rotation. The camera has a resolution of 1024 × 1024 pixels, which, for the field of view of the experiment, corresponded to a scaling factor of 6.81 pixels/cm. Each pair of images was taken at either 125 or 60 Hz, depending on the flow speed. Images were captured over a total of 59 turbine revolutions per case. This resulted in a total of 4248 image pairs per case that were later processed using DaVis imaging software (LaVision) for obtaining two-dimensional (2D) PIV measurements. Figure 7 shows a top-view schematic of the PIV field of view relative to the mounting location of the turbine. The image plane was calibrated using a wire mesh

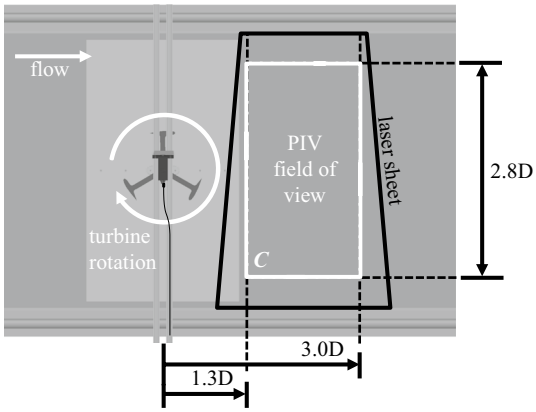

Fig. 7 Top-view schematic of the experimental setup. The contour, *C*, encloses the area that was used to calculate spatial averages of velocity as well as circulation. *Dashed vertical lines* indicate the relative position of *C* to the turbine center

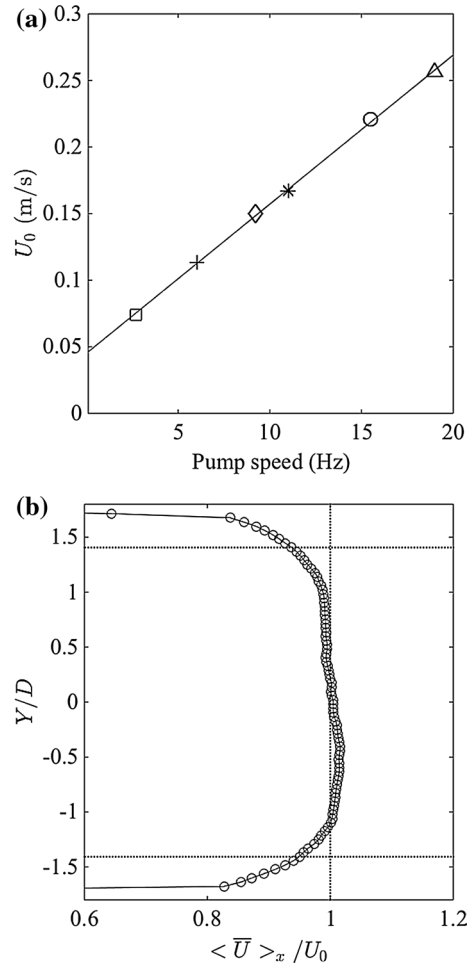

Fig. 8 **a** Measured freestream flow speeds, U_0, for different pump speed settings (*symbols*). The *solid line* is a linear fit to the points. **b** A sample of the measured streamwise velocity (*symbols*) for a pump setting of 15.5 Hz. The velocity has been averaged both in time and in the streamwise direction, indicated as $\langle \overline{U} \rangle_x$. The spanwise coordinate, *Y*, is normalized by the turbine diameter, *D*. *Dashed lines* are for reference only. The *upper* and *lower dashed lines* indicate the bounds of the contour, *C* (c.f. Fig. 7)

with equally spaced 2.54 cm squares. A multi-pass PIV algorithm was used with a decreasing interrogation window size and 50 % window overlap. Two passes were made with 32 × 32-pixel interrogation windows, followed by another two passes made with 16 × 16-pixel windows, the latter of which corresponded to vector spacing of 1.2 cm. A median filter with universal outlier detection was used to remove spurious vectors, which were subsequently replaced by interpolation.

To measure the nominal speed of the flow at the measurement location, PIV measurements were taken as described above, but with the turbine removed. The resulting streamwise velocity field was averaged in time as well as in the spanwise and streamwise directions to give a single-point measurement of the freestream flow speed. Measurements of six different flow speeds, each at a different pump speed, resulted in a linear regression with an R^2 value of 0.9993, as indicated in Fig. 8a. The derived linear equation from these measurements was used to calculate all of the subsequent freestream speeds. A sample of the freestream streamwise velocity profile is shown in Fig. 8b corresponding to a pump speed of 15.5 Hz. Boundary layers are observed to form near the walls of the channel. Their effect is partially negated by considering only velocity measurements away from the wall, i.e., within the contour, *C* (c.f. Fig. 7). In addition, since these wall effects (as well as turbine blockage) are always present, their effect is negligible when comparing similar flow-driven and motor-driven cases.

As a check for consistency, the flow speed was actively monitored during each test using a current velocity meter (Swoffer model 2100) placed upstream of the turbine. This flowmeter has a measurement range of 0.03–7.5 m/s and was calibrated using a moving cart system equipped with a laser distance sensor (see details in, e.g., Whittlesey and Dabiri 2013).

In flow-driven cases, the end shaft of the torque sensor was either freely spinning or slowed by a brake, as indicated in Fig. 9a.

Braking was achieved using a mechanical vise to adjust the amount of friction applied to the shaft and thus the average TSR of the turbine. In motor-driven cases, the end shaft of the torque sensor was connected to a DC motor (Pittman GM14904S013-R1), as indicated in Fig. 9b, and was controlled by a constant voltage power supply (Mastech HY3005F-3) capable of providing 0–30 V at 0–5 A. The static load of the motor, i.e., the torque due to its internal resistance, was such that at any flow speed the turbine could not rotate unless power was supplied to the motor.

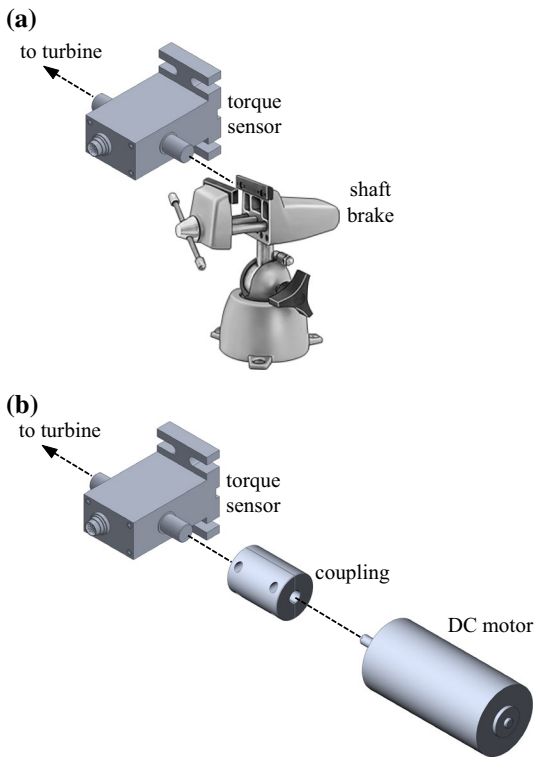

Fig. 9 Schematic of the setup used for controlling the turbine TSR in **a** flow-driven and **b** motor-driven cases

4 Experimental procedure

4.1 Turbine neutral curve

With the motor disconnected from the turbine and no additional load applied, the turbine performance was evaluated for the entire range of flow speeds of the facility. In each case, a LabView program tracked the number of turbine revolutions to compute the average TSR, as well as voltage measurements from the IR sensor, encoder, camera trigger, and torque sensor. All voltage measurements were sampled at 2500 Hz and recorded over a total of 59 turbine revolutions in each case. The average TSR over four trials for each flow speed is shown in Fig. 10 versus the turbine diameter Reynolds number, Re_D. Also shown in the figure is a shaded region that bounds one standard deviation in the measurement of TSR, as estimated by standard error propagation analysis. This figure is referred to throughout as the 'neutral curve', and it represents an upper bound on TSR for flow-driven cases. Since the turbine system has inherent losses (e.g., due to imperfect bearings), this empirical curve is shifted lower than that would be theoretically possible in the presence of only airfoil lift and drag forces. Nevertheless, it is a useful reference to distinguish between motor-driven cases that operate at a TSR above and below the limits of the curve, as is done in this study and detailed in the next section.

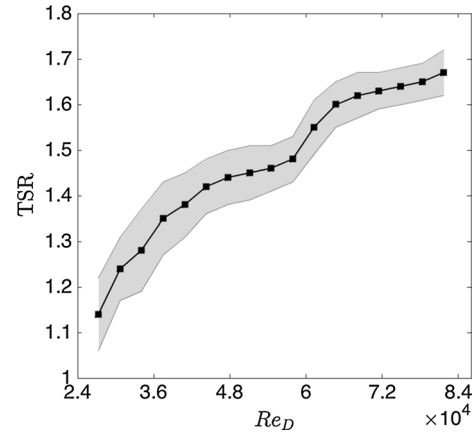

Fig. 10 Measured values (*symbols*) of the turbine neutral curve. The *shaded region* bounds one standard deviation in the measurement of TSR. The *neutral curve* indicates the maximum TSR that the turbine could reach for a given Re_D without an external load applied to its shaft

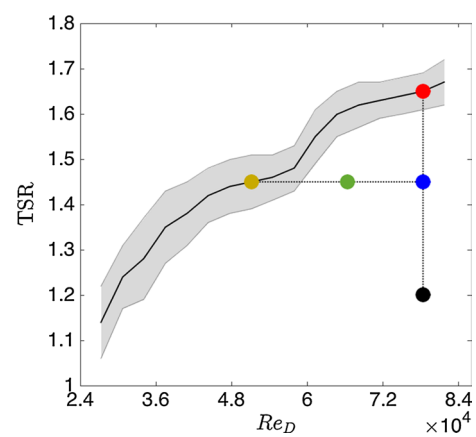

Fig. 11 Nominal turbine operating conditions (*symbols*) on or below the neutral curve (*solid black line*) selected for PIV measurements. The *yellow symbol* corresponds to $Re_D = 5.1 \times 10^4$, TSR = 1.45; the *green* to $Re_D = 6.6 \times 10^4$, TSR = 1.45; the *red*, *blue*, and *black* to $Re_D = 7.8 \times 10^4$ and TSR = 1.65, 1.45, and 1.20, respectively. The *dotted lines* are for visual reference only. The *shaded region* bounds one standard deviation in measured TSR along the neutral curve

4.2 PIV measurement conditions

Figures 11 and 12 indicate the nominal turbine operating conditions below and above the neutral curve, respectively. These were the conditions that were targeted for conducting PIV measurements of the wake.

The actual turbine operating conditions, measured during the PIV measurements, are indicated in Figs. 13 and 14; data in these figures are summarized in Tables 1 and 2, respectively. Below the neutral curve (c.f. Fig. 11), the selected turbine operating conditions included varying TSR for a fixed Re_D (red, blue, and black points), as well

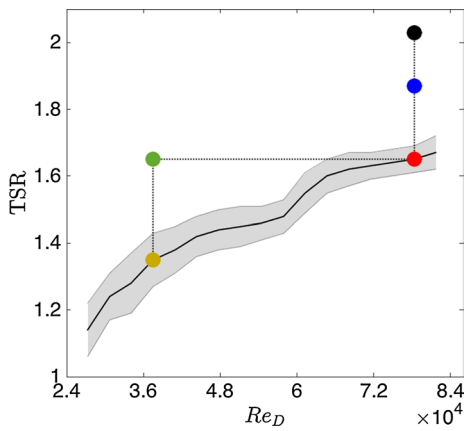

Fig. 12 Nominal turbine operating conditions (*symbols*) on or above the neutral curve (*solid black line*) selected for PIV measurements. The *yellow symbol* corresponds to $Re_D = 3.7 \times 10^4$, TSR = 1.35; the *green* to $Re_D = 3.7 \times 10^4$, TSR = 1.65; the *red*, *blue*, and *black* to $Re_D = 7.8 \times 10^4$ and TSR = 1.65, 1.87, and 2.03, respectively. The *dotted lines* are for visual reference only. The *shaded region* bounds one standard deviation in measured TSR along the neutral curve

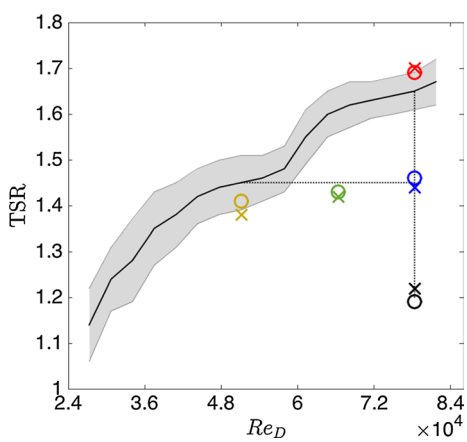

Fig. 13 Measured turbine operating conditions (*symbols*) on or below the neutral curve (*solid black line*) during PIV measurements. Symbols correspond to either flow-driven ('O') or motor-driven ('X') cases. Values for each symbol are given in Table 1. *Dotted lines* are for visual reference only and correspond to the nominal conditions (c.f. Fig. 11). The *shaded region* bounds one standard deviation in measured TSR along the neutral curve

as varying Re_D for a fixed TSR (green and yellow points). Above the neutral curve (c.f. Fig. 12), PIV measurements were taken for a fixed Re_D with varying TSR (red, blue, and black points), as well as two cases at a lower Re_D (green and yellow points). Of the latter two cases, the green point, which is motor-driven, was selected to match the TSR of the higher Re_D, flow-driven case (red point).

4.3 Calculation of wake statistics

The PIV measurements of the wake were used to examine both its steady and dynamic characteristics. To examine the steady-state behavior, spatiotemporal averages of the streamwise component of velocity, U, were examined. For each case, U was first averaged in time over the entire measurement period. A sample of the temporally averaged streamwise velocity, $\overline{U}$, is shown in Fig. 15. This temporal average was then spatially averaged in the spanwise (y) and streamwise (x) directions, denoted as $\langle \overline{U} \rangle_y$ and $\langle \overline{U} \rangle_x$, respectively, over the entire measurement domain bounded by the contour, C.

Wake dynamics were evaluated by computing the power spectra for the spanwise fluctuating velocity component, v', using the standard method of Welch (1967). The spectra for the flow-driven cases were computed at a single-point 1.3 turbine diameters (D) downstream of the turbine center and along the span where the rms of the velocity fluctuations was a maximum. This was typically near the edge of the wake, as indicated by the red circle in Fig. 15, where periodic blade vortex shedding would occur. The spectrum for a given motor-driven case was computed at the same point in the flow as in the corresponding flow-driven case. Since the turbine rotation rate fluctuated due to the unsteady hydrodynamic torque, the PIV data were not equally distributed in time, which is a necessary condition for spectral analysis. To account for this, the single-point velocity measurement was interpolated into an equally spaced vector in time before computing the spectra. Specifically, the time stamps for the 4248 velocity fields were determined using the camera trigger signal, which had a known sample rate of 2500 Hz. Each TTL pulse to the camera corresponded to one velocity field time stamp. These temporal data were used to perform a spline interpolation of the measured velocity fields to obtain 4500 interpolated velocity fields that were uniformly spaced in time and were used for computing the spectra. Figure 16 shows a sample of the measured (black line) and interpolated (red line) velocity data that correspond to the point in the flow indicated by the red circle in Fig. 15. It is worth noting that the computed spectra from this velocity data are limited by both the sample size and Nyquist frequency (i.e., half of the sample rate), which were both taken into consideration when plotting the spectra.

The circulation, Γ, in the wake of the turbine was evaluated by numerically integrating the vorticity within a rectangular area bounded by the contour, C (c.f. Fig. 15). By definition,

Table 1 Measured turbine operating conditions on or below the neutral curve during PIV measurements

Color	Symbol	Line	Driver	Re_D	TSR
Yellow	O	Solid	Flow	5.1×10^4	1.41
Yellow	X	Dashed	Motor	5.1×10^4	1.38
Green	O	Solid	Flow	6.6×10^4	1.43
Green	X	Dashed	Motor	6.6×10^4	1.42
Red	O	Solid	Flow	7.8×10^4	1.69
Red	X	Dashed	Motor	7.8×10^4	1.70
Blue	O	Solid	Flow	7.8×10^4	1.46
Blue	X	Dashed	Motor	7.8×10^4	1.44
Black	O	Solid	Flow	7.8×10^4	1.19
Black	X	Dashed	Motor	7.8×10^4	1.22

Symbols correspond to Fig. 13; linetypes correspond to Figs. 17, 18, 21, and 22

The 'driver' of the turbine rotation is indicated as either 'flow' for flow-driven or 'motor' for motor-driven

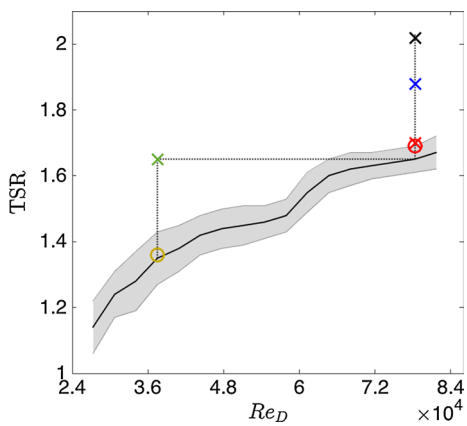

Fig. 14 Measured turbine operating conditions (*symbols*) on or above the neutral curve (*solid black line*) during PIV measurements. Symbols correspond to either flow-driven ('O') or motor-driven ('X') cases. Values for each symbol are given in Table 2. *Dotted lines* are for visual reference only and correspond to the nominal conditions (c.f. Fig. 12). The *shaded region* bounds one standard deviation in measured TSR along the neutral curve

Table 2 Measured turbine operating conditions on or above the neutral curve during PIV measurements

Color	Symbol	Line	Driver	Re_D	TSR
Red	O	Solid	Flow	7.8×10^4	1.69
Red	X	Dashed	Motor	7.8×10^4	1.70
Blue	X	Dashed	Motor	7.8×10^4	1.88
Black	X	Dashed	Motor	7.8×10^4	2.02
Yellow	O	Solid	Flow	3.7×10^4	1.36
Green	X	Dashed	Motor	3.7×10^4	1.65

Symbols correspond to Fig. 14; linetypes correspond to Figs. 23 and 24

The 'driver' of the turbine rotation is indicated as either 'flow' for flow-driven or 'motor' for motor-driven

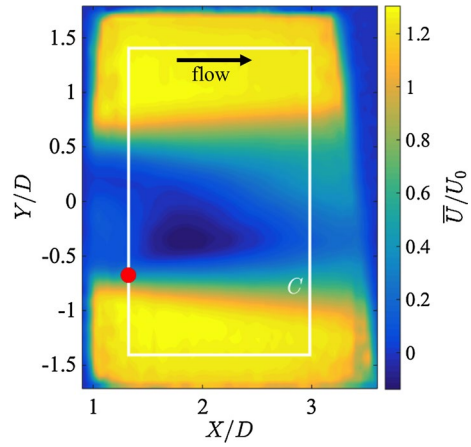

Fig. 15 Contour plot of the temporally averaged streamwise component of velocity, $\overline{U}$, corresponding to $Re_D = 7.8 \times 10^4$ and TSR = 1.69. The velocity is normalized by the freestream velocity, U_0, and X and Y are measured relative to the turbine center. The *rectangular contour*, C, encloses the area used to calculate spatial averages of velocity as well as circulation. At 1.3 D downstream of the turbine center, the *red circle* corresponds to the Y/D location where the rms of the transverse velocity fluctuations, v', was a maximum

$$\Gamma \equiv \iint_A \overline{\omega} \cdot \mathrm{d}\mathbf{A}, \tag{1}$$

where $\overline{\omega}$ is the vorticity derived from the temporally averaged velocity and d**A** is a differential area element.

4.4 PIV error analysis

Confidence bounds on the PIV measurements were estimated using a statistical technique called dependent circular block bootstrapping. Details of the method are given by Theunissen et al. (2008). To summarize, at each point in the flow, the 4500 velocity samples were divided into overlapping blocks, where the block length for a given case was specified by the degree of autocorrelation among the samples. The blocks were then randomly sampled with replacement to construct a new series of 4500 velocities, called the bootstrap series. It is with this bootstrap series that any desired statistic can be calculated, e.g., the mean. Repeating this a number of times gives an estimate of the confidence bounds for a given statistic. For normally distributed data, the bootstrap estimate of a given statistic tends to converge toward its 'true' value by increasing the number of bootstrap series used to calculate this statistic. Note that this error estimate does not account for any systematic error in the experimental method itself, but is sufficient for a comparative analysis, as in the case of this study. For the current PIV data set, a total of 5000 bootstrap series were created for each point in the flow. From these, the temporal mean and standard deviation were calculated and then

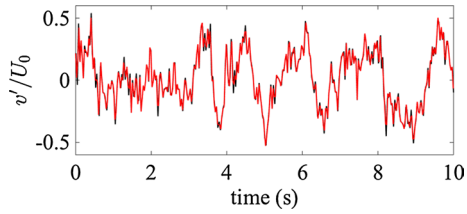

Fig. 16 Sample of the measured spanwise fluctuating velocity component, v', normalized by the freestream velocity, U_0. The velocity sample corresponds to the point in the flow indicated by the *red circle* in Fig. 15. The *black line* indicates the velocity as measured from PIV, and the *red line* is the interpolated velocity used to compute the spectra

averaged in space corresponding to either the spanwise or streamwise averages of velocity. For all cases examined, the bootstrap estimate of error in each calculated spatiotemporal average of the measured velocity was approximately 2 % of the freestream velocity with 95 % confidence.

5 Results

5.1 PIV measurements on or below the neutral curve

The spatiotemporal average velocity measurements corresponding to the operating conditions given in Table 1 are shown in Figs. 17 and 18, where solid lines indicate flow-driven conditions, and dashed lines indicate motor-driven conditions.

Representative error bars are only drawn at the beginning and end of each curve in the figures so as not to obscure the data. In all instances, there appears to be close agreement among the flow-driven and motor-driven cases. There also appears to be a strong dependence of the wake velocity on TSR, while relatively little dependence on Reynolds number, as indicated by the overlapping velocity profiles in Fig. 18. This weak Reynolds number dependance is consistent with the previous results of Bachant and Wosnik (2014). It is interesting to note in Fig. 17a a change in the trend of the velocity recovery as TSR increases. Just behind the turbine (i.e., $X/D < 1.5$) as TSR is increased from approximately 1.2 (black curve) to 1.5 (blue curve), the velocity decreases. However, as TSR is increased further from approximately 1.5 (blue curve) to 1.7 (red curve), the velocity increases in this region. It is speculated that this change in the velocity recovery could be due to the influence of TSR on the vortices shed from the turbine, similar to the suppression of vortices observed by Chan et al. (2011) in the wake of spinning cylinders.

To more closely inspect the spatial development of the velocity profile, spanwise sections of the time-averaged velocity are shown in Fig. 19 for a fixed Re_D and TSR.

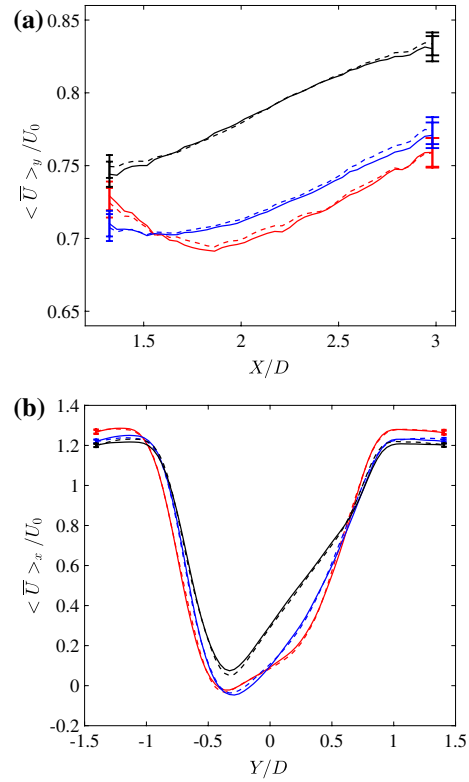

Fig. 17 Spatiotemporal average velocity in the **a** spanwise and **b** streamwise direction when Re_D is fixed and TSR is varied. *Solid lines* indicate flow-driven conditions and *dashed lines* indicate motor-driven conditions. *Colors* correspond to the nominal operating conditions on or below the neutral curve, i.e., $Re_D = 7.8 \times 10^4$ and TSR = 1.65 (*red*), 1.45 (*blue*), and 1.20 (*black*). The measured conditions for each line are given in Table 1. *Error bars* indicate one standard deviation

Additionally, the corresponding Reynolds stresses are shown in Fig. 20 for the same conditions as in Fig. 19.

In both Figs. 19 and 20, there is reasonable agreement observed between flow-driven and motor-driven conditions, indicated by overlapping symbols that are connected by either solid (flow-driven) or dotted (motor-driven) lines. Comparing Figs. 17 and 19, it is interesting to observe the similarity between the trend in the streamwise development of the velocity profile and the TSR dependance of the spatial averages. Specifically, it appears that increasing the TSR leads to a greater velocity deficit that occurs further downstream, thus delaying the onset of its recovery. Examining Figs. 19 and 20, it is evident that the spanwise asymmetry in the velocity profile is reflected in the asymmetry of the spanwise Reynolds stress distributions. There are two peaks in both the longitudinal and shear Reynolds stresses (i.e., $\langle u'u' \rangle$ and $\langle u'v' \rangle$, respectively) that differ in magnitude and occur on either side of the minimum wake velocity. This minimum velocity is shifted away from the centerline of the channel in the direction of the maximum

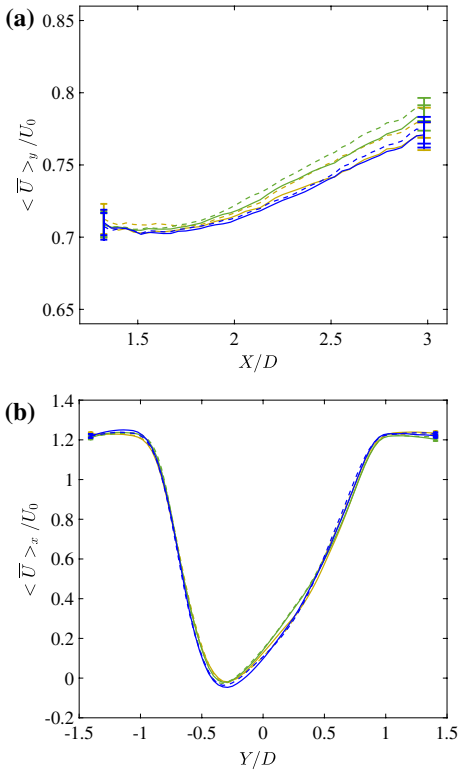

Fig. 18 Spatiotemporal average in the **a** spanwise and **b** streamwise direction when Re_D is varied and TSR is fixed. *Solid lines* indicate flow-driven conditions, and *dashed lines* indicate motor-driven conditions. *Colors* correspond to the nominal operating conditions on or below the neutral curve, i.e., TSR = 1.45, $Re_D = 5.1 \times 10^4$ (*yellow*), $Re_D = 6.6 \times 10^4$ (*green*), $Re_D = 7.8 \times 10^4$ (*blue*). The measured conditions for each line are given in Table 1. *Error bars* indicate one standard deviation

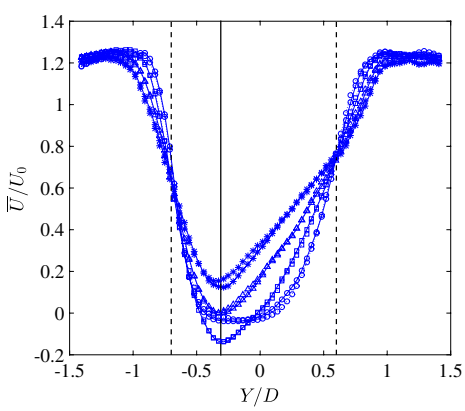

Fig. 19 Time-averaged streamwise velocity, $\overline{U}$, at (○) $X/D = 1.3$; (*square*) $X/D = 1.9$; (*triangle*) $X/D = 2.5$; and (*asterisk*) $X/D = 3.0$. Symbols connected by a *solid line* correspond to flow-driven conditions, and those connected by a *dotted line* correspond to motor-driven conditions; both are nominally $Re_D = 7.8 \times 10^4$ and TSR = 1.45. *Dashed vertical lines* correspond to dominant peaks in the Reynolds stress distributions (c.f. Fig. 20), i.e., at $Y/D = -0.7$ and $Y/D = 0.6$. The *solid vertical line* corresponds to the minimum velocity at $Y/D = -0.3$

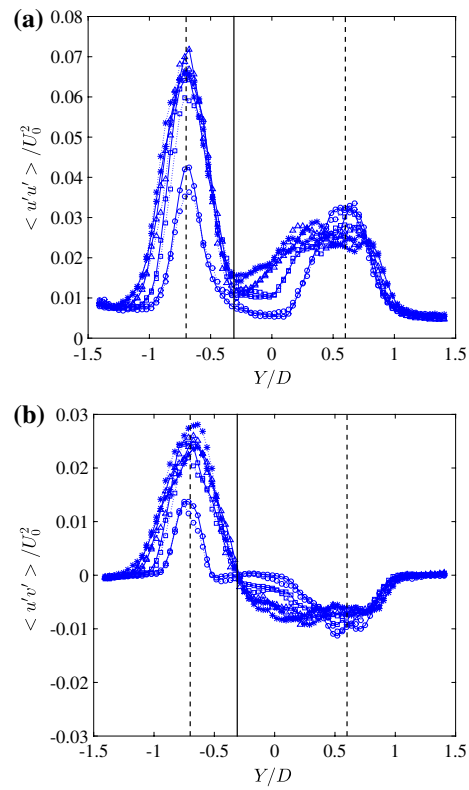

Fig. 20 **a** Longitudinal and **b** shear Reynolds stress. All *symbols* correspond to those of Fig. 19. *Dashed vertical lines* correspond to dominant peaks in the Reynolds stress distributions, i.e., at $Y/D = -0.7$ and $Y/D = 0.6$. The *solid vertical line* corresponds the minimum velocity at $Y/D = -0.3$

Reynolds stress (i.e., at $Y/D = -0.3$). It is thought that this asymmetry in the wake is initiated by a stronger shear layer that forms on the side of the turbine where the blades advance upstream.

The velocity power spectra for the same cases as discussed above are shown in Figs. 21 and 22.There is again reasonable agreement among the flow-driven and motor-driven cases, indicated by the overlap of the solid and dashed spectral distribution curves. This implies that the underlying vortex dynamics in the wake are virtually unaffected by the use of the motor to mimic the flow-driven turbine kinematics. It is also of interest to note the effect of TSR on the distribution of the spectra. Specifically, there appears to be both a broadening and a shift of the largest spectral peak toward lower frequencies with increasing TSR, as can be observed between Fig. 21 (a) and (b). The broader peak suggests more diffuse vortex structures, which is consistent with an earlier decay of shed vortices. Also, since the spectra were sampled at the same *X/D* location, it further indicates that the TSR plays a role in the spatial development of these structures, as noted earlier when examining the spatially and temporally averaged velocity

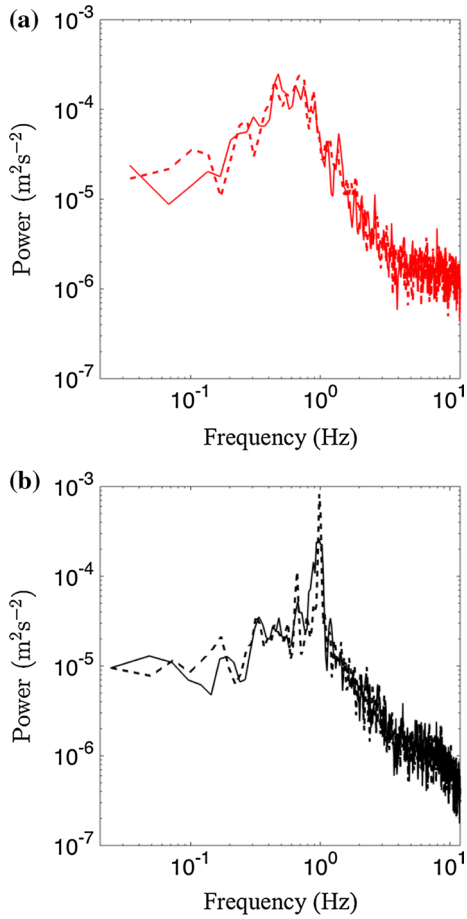

Fig. 21 Power spectra for the spanwise fluctuating velocity component, v', in flow-driven (*solid lines*) and motor-driven (*dashed lines*) cases. *Colors* correspond to the nominal operating conditions on or below the neutral curve, i.e., $Re_D = 7.8 \times 10^4$, TSR = 1.65 (*red*) and 1.20 (*black*). The measured conditions for each line are given in Table 1

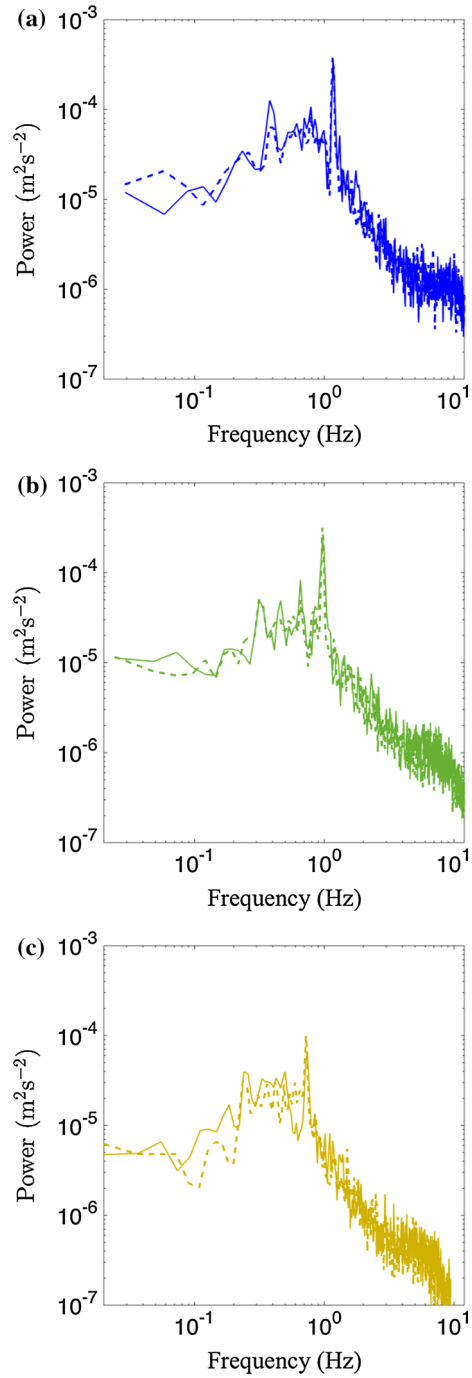

Fig. 22 Power spectra for the spanwise fluctuating velocity component, v', in flow-driven (*solid lines*) and motor-driven (*dashed lines*) cases. *Colors* correspond to the nominal operating conditions on or below the neutral curve, i.e., TSR = 1.45, $Re_D = 7.8 \times 10^4$ (*blue*), 6.6×10^4 (*green*), and 5.1×10^4 (*yellow*). The measured conditions are given in Table 1

profiles. In contrast, the spectral distributions look qualitatively similar between Fig. 22a–c, in which the TSR is nearly identical but Re_D differs.

5.2 Measurements on or above the neutral curve

The spatiotemporal average velocity measurements corresponding to the operating conditions given in Table 2 are shown in Figs. 23 and 24.

Above the neutral curve, it is not possible to directly compare motor-driven with flow-driven cases as was done previously. However, it is still interesting to note from Fig. 23 that the shape of the velocity profile continues to be a strong function of TSR in this regime.

Figure 24 shows a comparison of the velocity profiles between two flow-driven cases along the neutral curve, but at different Reynolds numbers, and one motor-driven case above the neutral curve that attempts to match the TSR of the higher Reynolds number, flow-driven case. A somewhat surprising result is that the velocity profile for the motor-driven turbine (dashed green line), operating above the neutral curve, is close to matching the profile of the

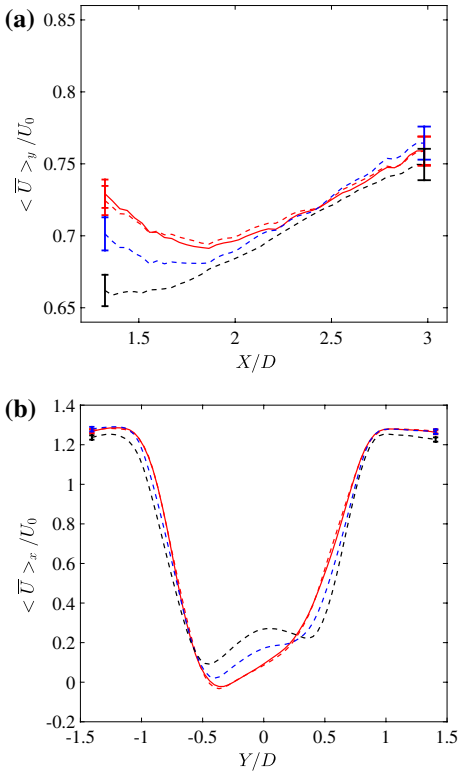

Fig. 23 Spatiotemporal average velocity in the (a) spanwise and (b) streamwise direction when Re_D is fixed and TSR is varied. *Solid lines* indicate flow-driven conditions, and *dashed lines* indicate motor-driven conditions. Colors correspond to the nominal operating conditions on or above the neutral curve, i.e., $Re_D = 7.8 \times 10^4$ and TSR = 1.65 (*red*), 1.88 (*blue*), and 2.02 (*black*). The measured conditions for each line are given in Table 2

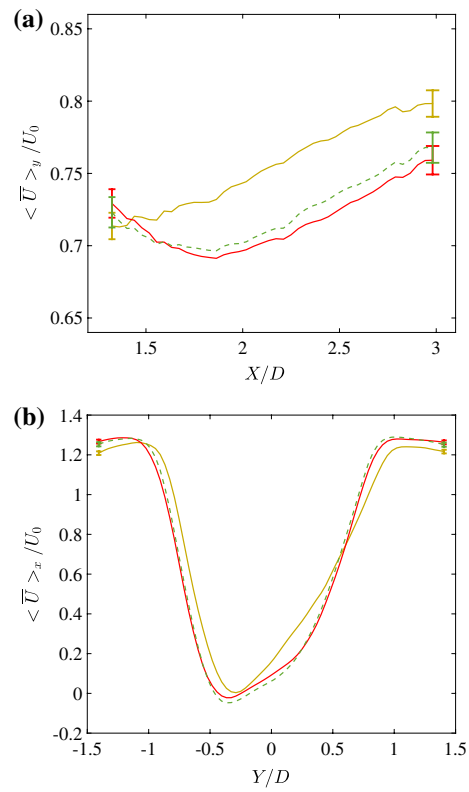

Fig. 24 Spatiotemporal average in the, **a** spanwise and **b** streamwise direction when both Re_D and TSR are varied. *Solid lines* indicate flow-driven conditions, and *dashed lines* indicate motor-driven conditions. *Colors* correspond to the nominal operating conditions on or above the neutral curve, i.e., $Re_D = 7.8 \times 10^4$ and TSR = 1.65 (*red*), $Re_D = 3.7 \times 10^4$ and TSR = 1.36 (*yellow*), $Re_D = 3.7 \times 10^4$ and TSR = 1.65 (*green*). The measured conditions are given in Table 2

flow-driven turbine (solid red line) at nearly the same TSR but higher Reynolds number. The implications of this result are discussed in the next subsection.

5.3 Circulation and torque measurements

Figure 25 presents wake circulation measurements for a fixed $Re_D = 7.8 \times 10^4$ and TSR ranging from approximately 0.9–2.8. There is qualitative agreement in the trend of the net circulation for similar flow-driven and motor-driven cases, though there are slight magnitude differences observed that could not be established conclusively at the precision level of the experiment.

Interestingly, there is a change in sign in the circulation near TSR ≈ 2, which is above the empirically measured free-spin limit of the turbine at this Reynolds number, which was TSR ≈ 1.7. This suggests that just beyond the empirical TSR limit, the motor acts to overcome losses in the turbine system, while the turbine blades continue to

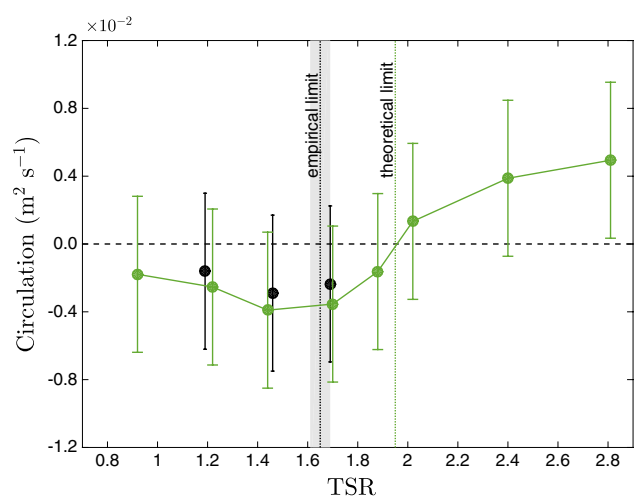

Fig. 25 Measured circulation for flow-driven (*black*) and motor-driven (*green*) cases. *Error bars* represent an estimate of one standard deviation in measurement error. Motor-driven points are connected with *straight-line* segments

produce net torque due to lift. Beyond the zero crossing in circulation, the turbine blades produce net torque due to drag, which results in wake measurements that are qualitatively different from a flow-driven turbine. Therefore, the zero crossing in circulation represents a measure of the theoretical maximum TSR for a motor-driven turbine, below which wake measurements will agree with that of a corresponding flow-driven turbine.

An interesting consequence of this result is that the motor-driven case at TSR = 1.88 (blue curve) in Fig. 23, which had no corresponding flow-driven case for comparison, can now be considered as a legitimate representation of the flow-driven turbine wake, assuming it could overcome the losses inherent to its system. Additionally, though it is not shown in Fig. 25, a check of the circulation for the motor-driven case above the neutral curve (green dashed line) in Fig. 24 gives a value of approximately $-0.2 \times 10^{-2}\ \mathrm{m^2\,s^{-1}}$. This negative value indicates that the turbine blades are still producing net lift for this case, which is consistent with the observed agreement between the flow-driven (solid red line) and motor-driven (dashed green line) velocity profiles. However, the wake corresponding to the motor-driven case at TSR = 2.02 is unphysical as a representation of a flow-driven turbine.

Turbine shaft torque measurements are shown in Fig. 26 for the same flow conditions as the circulation in Fig. 25. There is again good agreement between flow-driven and motor-driven torque measurements. However, the change in sign in torque occurs at an earlier TSR than that which was indicated by circulation. This is not surprising given that no effort was made to quantify the torque due to losses in the turbine system. Howell et al. (2010) note that in small-scale VAWT experiments, the power loss due to bearing friction and windage can be very significant and is a complex function of TSR. For low TSR, they report nearly 50 % of the total torque produced by the turbine is lost to the bearings, support arms and windage in the system; for high TSR, these losses were nearly double the torque produced by the turbine. For this reason, the zero crossing in torque provides a conservative estimate of the theoretical maximum TSR for a motor-driven turbine to still give reliable wake measurements.

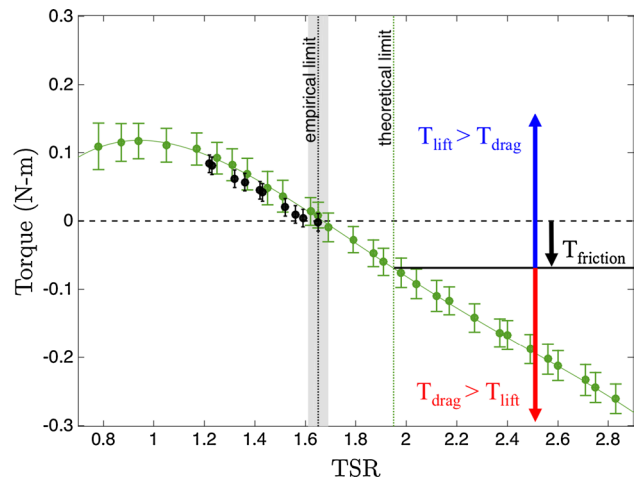

Fig. 26 Measured torque for flow-driven (*black*) and motor-driven (*green*) cases. *Error bars* represent an estimate of one standard deviation in measurement error. A fourth-order polynomial is fit to the motor-driven points

6 Conclusion

These results demonstrate the existence of a finite region in TSR versus Re number space where a motor-driven turbine can reproduce the physics of a flow-driven turbine. That region extends beyond the free-spin limit of the flow-driven turbine, which is hindered by frictional losses. It was shown that this region is bounded by a sign change in the net circulation of the wake above a TSR threshold, indicating a transition from net torque due to lift to net torque due to drag produced by the turbine blades. Shaft torque measurements support this conclusion by also showing a sign change above the TSR threshold set by circulation. However, not accounting for torque losses due to bearing friction and windage leads to a zero crossing in the torque measurement at a lower TSR than that is thought to be theoretically possible, making this a more conservative estimate of the TSR limit (see 'T_{friction}' in Fig. 26). At or below this TSR limit, wake measurements agree between a motor-driven turbine and that of a corresponding flow-driven turbine. Further increasing TSR beyond this limit, however, leads to the turbine operating in a drag-dominated regime, which gives wake measurements that are inconsistent with a flow-driven turbine.

A notable feature of the wake evaluated in this study is a spanwise asymmetric velocity profile. This is attributed to a stronger shear layer that develops on the side of the turbine where the blades advance upstream and are reflected in an asymmetric Reynolds stress distribution across the span. The velocity in the wake, both averaged and time-varying, was found to be strongly dependent on TSR and only weakly dependent on Reynolds number. Increasing the TSR was found to create a larger velocity deficit with the minimum velocity shifted downstream.

The conclusions of this work suggest that the turbine kinematics and aerodynamic properties are the sole factors

that govern the dynamics of its wake, irrespective of the means to move the turbine blades. This implies that investigations where turbine blade kinematics is prescribed are justified, and may even allow greater flexibility in experiments where inherent system losses hinder the operational conditions of interest. However, future studies in which turbine rotation is prescribed (either in experiments or numerically) should examine the behavior of the net torque and or wake circulation to confirm that the results are physically meaningful for studies of turbine fluid mechanics.

Acknowledgments This work was funded by an NSF Graduate Research Fellowship as well as the Caltech Resnick Institute Graduate Fellowship to D.B.A. Funding to J.O.D. from the Gordon and Betty Moore Foundation through Grant No. GBMF2645 and the Office of Naval Research through Grant N000141211047 are also gratefully acknowledged.

Appendix

See Table 3.

References

Bachant P, Wosnik M (2014) Reynolds number dependence of cross-flow turbine performance and near-wake characteristics. In: Proceedings of the 2nd Marine energy technology symposium, Seattle

Bahaj A, Batten W, McCann G (2007) Experimental verifications of numerical predictions for the hydrodynamic performance of horizontal axis marine current turbines. Renew Energ 32:2479–2490

Battisti L, Zanne L, Anna SD (2011) Aerodynamic measurements on a vertical axis wind turbine in a large scale wind tunnel. J Energ Resour 133:031201

Bazilevs Y, Hsu MC, Kiendl J, Wüchner R, Bletzinger KU (2011) 3D simulation of wind turbine rotors at full scale. Part II: fluid-structure interaction modeling with composite blades. Int J Numer Methods Fluids 65:236–253

Cal RB, Lebrón J, Castillo L, Kang HS, Meneveau C (2010) Experimental study of the horizontally averaged flow structure in a model wind-turbine array boundary layer. J Renew Sustain Energy 2:013106

Chamorro LP, Arndt REA, Sotiropoulos F (2011) Turbulent flow properties around a staggered wind farm. Bound-Lay Meteorol 141:349–367

Chan AS, Dewey PA, Jameson A, Liang C, Smits AJ (2011) Vortex suppression and drag reduction in the wake of counter-rotating cylinders. J Fluid Mech 679:343–382

Chao DD, van Dam CP (2007) Computational aerodynamic analysis of a blunt trailing-edge airfoil modification to the NREL Phase VI rotor. Wind Energy 10:529–550

Table 3 Summary of selected wind turbine experimental and numerical studies

	HAWT	VAWT	Numerical	Experimental	Flow-driven	Motor-driven	Torque/power reported
Ebert and Wood (1997)	X			X	X		X
Grant and Parkin (2000)	X			X	X		
Xu and Sankar (2000)	X		X			X	
Fujisawa and Shibuya (2001)		X		X		X	
Duque et al. (2003)	X		X			X	X
Bahaj et al. (2007)	X		X	X	X	X	X
Chao and Dam (2007)	X		X			X	X
Lida et al. (2007)		X	X			X	X
Ferreira et al. (2009)		X		X		X	
Howell et al. (2010)		X	X	X	X	X	X
Cal et al. (2010)	X			X	X		X
Battisti et al. (2011)		X		X	X		X
Bazilevs et al. (2011)	X		X		X		X
Chamorro et al. (2011)	X			X	X		
Hsu and Bazilevs (2012)	X		X		X		X
Li et al. (2012)		X	X			X	
Martinelli and Smits (2012)		X	X			X	X
Bachant and Wosnik (2014)		X	X	X	X	X	X
Korobenko et al. (2014)		X	X			X	X
Le et al. (2014)		X	X		X	X	X
Nini et al. (2014)		X	X			X	
Shamsoddin and Porté-Agel (2014)		X	X			X	
Tescione et al. (2014)		X		X		X	

Duque EP, Burklund MD, Johnson W (2003) Navier-Stokes and comprehensive analysis performance predictions of the NREL phase VI experiment. J Sol Energ 125:457–467

Ebert PR, Wood D (1997) The near wake of a model horizontal-axis wind turbine—I. Experimental arrangements and initial results. Renew Energ 12:225–243

Ferreira CS, van Kuik G, van Bussel G, Scarano F (2009) Visualization by PIV of dynamic stall on a vertical axis wind turbine. Exp Fluids 46:97–108

Fujisawa N, Shibuya S (2001) Observations of dynamic stall on Darrieus wind turbine blades. J Wind Eng Ind Aerod 89:201–214

Grant I, Parkin P (2000) A DPIV study of the trailing vortex elements from the blades of a horizontal axis wind turbine in yaw. Exp Fluids 28:368–376

Howell R, Qin N, Edwards J, Durrani N (2010) Wind tunnel and numerical study of a small vertical axis wind turbine. Renew Energ 35:412–422

Hsu MC, Bazilevs Y (2012) Fluid-structure interaction modeling of wind turbines: simulating the full machine. Comput Mech 50:821–833

Kang HS, Meneveau C (2010) Direct mechanical torque sensor for model wind turbines. Meas Sci Technol 21:105206

Korobenko A, Hsu MC, Akkerman I, Bazilevs Y (2014) Aerodynamic simulation of vertical-axis wind turbines. J Appl Mech 81:021011

Le TQ, Lee KS, Park JS, Ko JH (2014) Flow-driven rotor simulation of vertical axis tidal turbines: a comparison of helical and straight blades. Int J Nav Archit Ocean Eng 6:257–268

Li ZC, Sheng QH, Zhang L, Cong ZM, Jiang J (2012) Numerical simulation of blade-wake interaction of vertical axis tidal turbine. Adv Mat Res 346:318–323

Lida A, Kato K, Mizuno A (2007) Numerical simulation of unsteady flow and aerodynamic performance of vertical axis wind turbines with LES. In: Proceedings of the 16th Australasian fluid mechanics conference. Crown Plaza, Gold Coast

Martinelli L, Smits AJ (2012) High-fidelity computational fluid dynamics (CFD) for the wind/tidal energy industry. In: Proceedings of the HKIE civil division international conference, Hong Kong

Nini M, Motta V, Bindolino G, Guardone A (2014) Three-dimensional simulation of a complete vertical axis wind turbine using overlapping grids. J Comput Appl Math 270:78–87

Shamsoddin S, Porté-Agel F (2014) Large eddy simulation of vertical axis wind turbine wakes. Energies 7:890–912

Tescione G, Ragni D, He C, Ferreira CJS, van Bussel G (2014) Near wake flow analysis of a vertical axis wind turbine by stereoscopic particle image velocimetry. Renew Energ 70:47–61

Theunissen R, Sante AD, Riethmuller ML, den Braembussche RAV (2008) Confidence estimation using dependent circular block bootstrapping: application to the statistical analysis of PIV measurements. Exp Fluids 44:591–596

Welch PD (1967) The use of fast Fourier transform for the estimation of power spectra: a method based on time averaging over short, modified periodograms. IEEE Trans Audio Electroacoust 15:70–73

Whittlesey RW, Dabiri JO (2013) Optimal vortex formation in a self-propelled vehicle. J Fluid Mech 737:78–104

Xu G, Sankar LN (2000) Computational study of horizontal axis wind turbines. J Sol Energ 122:35–39